Ultra-Compact Tuneable Notch Filter Using Silicon Photonic Crystal Ring Resonator

Ultra-compact tuneable notch filter using silicon photonic crystal ring resonator

G. Brunetti, F. Dell'Olio, D. Conteduca, M. N. Armenise,
C. Ciminelli, *Senior Member, IEEE, Senior Member, OSA*

***Abstract*—A novel ultra-compact photonic tuneable notch filter with large bandwidth, high extinction ratio, fast response, and flat stopband, is modelled and designed. It consists of a silicon-based ring resonator with one-dimensional photonic crystal superimposed onto a ring portion. Engineering the defects into the photonic crystal section allows to achieve the equalization of the bottom band of the filter response. Large bandwidth (*B* = 10.43 GHz) and high extinction ratio (*ER* = 41 dB) have been attained with a frequency response of the 1st order Butterworth filter type. Continuous and wide range tunability of the central frequency (15 GHz) has been obtained by using the carrier injection technique, together with fast reconfigurability (≈ 1 ns) and power consumption of 47 mW. The device footprint is as very small as about 150 μm^2. This performance makes the proposed device suitable for several filtering applications, such as wireless networks (5G) and telecommunication reconfigurable payloads in Telecom and Space scenario, respectively.**

***Index Terms*— Bragg gratings, Optical filters, Optical resonators.**

I. Introduction

Optical filtering is useful in several application fields, due to its advantages over the conventional RF techniques, such as wide tunability, fast reconfigurability, very small footprint, large bandwidth, high extinction ratio, flat stopband and immunity to electromagnetic interference.

In the Telecom scenario, optical filters are key devices for WDM systems, assuming the major role in the gain equalization and the dispersion compensation [1]. In the last few years, a big research effort has been focused on optical filters for the next generation wireless telecommunications systems that require high capability, flexibility, compactness and multiband networks. They are indeed building blocks in the Microwave Photonics (MWP), a key enabling technology of future wireless networks [2-4]. The use of optical filters in RF sub-systems opens up the chance of pre-filtering in the optical domain before the analog-to-digital conversion, in order to facilitate the subsequent digital signal processing [5]. In Space applications, such as radar and phased-array-antennas in telecom satellite payloads, the use of optical filtering fits the requirements of payload adjustments and optimization after the launch, in terms of bandwidth, coverage and frequency allocation [6,7].

Optical filters with an almost ideal rectangular spectrum, reconfigurable and with a multiband operation, which is often very challenging to provide with conventional electronics, are needed in several applications, where the system performance strongly depends on the response of the optical filter.

An optical filter can be realized by using either a discrete or monolithic approach. The former approach is typically exploited by photonic filters based on optical fibres and bulk optical components, but it suffers from thermal and mechanical instability, together with other drawbacks in terms of size, weight, power and cost [8]. The monolithic integration provides stable and compact structures, and several filters have been recently proposed in various integration platforms for telecom and microwave photonic applications [9-11]. The use of low loss waveguides integrated in passive systems allows to minimize the insertion loss and to avoid any change of the filter characteristics due to the device tuning. Assuming a high extinction ratio and a rapid roll-off as the target for notch filters, the most remarkable limitation is the poor flatness of the passband due to the Lorentz-shape of the optical notch spectral response, typically observed also in the high performance microwave photonic filters (MPFs). A flat band is required in order to filter all spectral components in the bandwidth with the same attenuation coefficient. Several integrated solutions have been proposed in literature to increase the band-flatness of the notch and/or pass-band response, mostly by using microring resonators (MRRs) [12-17], Bragg gratings (BGs) [18-21] or Mach-Zehnder interferometers (MZI) [22].

A Gaussian shaped resonance with a pass band ripple less than 0.5 dB has been demonstrated by using more than two MRRs [13]. In particular, a pass-band/notch bandwidth of 1.9 GHz with a footprint of 1.23 mm^2 has been demonstrated with five series coupled MRRs [13], while 40 cascaded MRRs have demonstrated a tuneable and flat bandwidth of 20-100 GHz [15]. However, while a complex configuration of MRRs enables a flat bandwidth, the use of multiple MRRs requires a larger chip area, with consequent higher insertion losses, and more challenging device manufacturing. A substantial dependence on the performance parameters of the MRRs, i.e. the coupling efficiency and the optical path length, results. Huang *et al.* [16] proposed a solution based on an electrically tuned single microring and a reflector. The device can provide a flat notch or pass-band filter, exploiting the fast and slow light effect, respectively. The filter shows a -3 dB bandwidth of 7.5 GHz and a footprint of 0.47 mm^2, far from meeting the requirements of large bandwidth and compactness.

G. Brunetti F. Dell' Olio, M. N. Armenise and C. Ciminelli are with Optoelectronics Laboratory, Politecnico di Bari, Bari 70125 Italy (e-mail: caterina.ciminelli@poliba.it).

D. Conteduca was with Optoelectronics Laboratory, Politecnico di Bari, Bari 70125 Italy. He is now with Photonics Group, Department of Physics, University of York, Heslington, York YO10 5DD, United Kingdom.

Bragg gratings-based configurations have been proposed in literature to overcome such limitation. A Silicon on Insulator (SOI) Bragg grating, 800 μm long, has been proposed as a notch filter, obtaining a bandwidth of about 100 GHz, a ripple of about 1 dB and an insertion loss of 0.5 dB [18]. Recently, a thermally tuneable grating used as optical filter and based on a suspended silicon ridge waveguide has been proposed [19], verifying experimentally low power consumption (power efficiency of ~300 pm/mW) and fast response (tens of microseconds).

Simultaneous pass-band and notch filter functions can be realized with more complex Bragg gratings-based configurations [20,21]. In particular, superimposing Bragg gratings on the two arms of a 2x2 Mach-Zehnder interferometer, the measured notch/passband filtering shape at through/drop port shows high rejection ratio (about 15 dB), high flatness (ripple < 0.5 dB for the pass-band shape, ripple ≈ 10 dB for the notch shape) and bandwidth of about 50 GHz [20]. Recently, Jiang *et al*. [21] have proposed a complex flat broadband tuneable silicon filter, based on waveguide Bragg gratings, enabling both pass-band and notch operation. The structure is 500 μm long and provides a wide filtering bandwidth of a few THz. The measured ripple of the passband shape is less than 0.5 dB, but the notch filtering response shows a ripple of about 5 dB.

As already mentioned, a wide tunability of the central frequency is a crucial aspect for the optical filtering. An electromechanical [17] and thermo-optical [12,13] tuning have been already investigated in literature. The electromechanical tuning is strictly related to the deflection of a cantilever [17], providing a central wavelength shift of a few GHz with a power consumption in the order of hundreds of nW.

The thermo-optic tuning mechanism of a filter based on ring resonators produces a large wavelength shift (of the order of tens GHz), low optical loss [13] with a power consumption of a few mW for simple configurations [12] and tens of mW (≈ 70 mW) for complex geometries [13]. However, the switching time (tens of μs) and the thermal cross-talk between multiple resonators affect its use in highly dense integrated optical systems [12]. However, although the electromechanical approach ensures a reasonable filter shift with low power consumption, the slow switching time and the manufacturing complexity limit its use. On the contrary, even if the thermo-optic mechanism is characterized by ease of manufacturing, this approach presents some issues related to the thermal crosstalk and the slow switching time.

The electro-optic tuning mechanism can be used to avoid, or at least to mitigate, the aforementioned issues, typical of the thermal and electromechanical tuning. The electro-optic tuning is based on the free-carrier-plasma-dispersion, that provides a switching time less than 1 ns [23,24], together with the capability of integrating electro-optic devices with CMOS circuits.

In this paper, we propose the design of an ultra-compact and tuneable 1st order Butterworth notch filter with a narrow and flat-bottom passband, based on a photonic crystal ring resonator (PhCRR). The optimized design of the defective photonic crystal allows to achieve the Gaussian shaping of the PhCRR frequency response, with a flat bottom band (with a ripple of about 0.5 dB). A bandwidth B ~ 10 GHz has been obtained together with a very small device footprint (~ 147 μm^2). By exploiting the electro-optic effect based on the free-carrier-plasma-dispersion as tuning mechanism, the frequency response could be tuned in a range of 15 GHz, where any changes in the spectral response are prevented, with a reconfigurability time less than 1 ns and a good enough power consumption of about 47 mW. The PhCRR filter we propose is the first ultra-compact solution with narrow and flat stopband, wide range and fast tunability and integration capability, to our knowledge. The performance of our device makes it particularly suitable for some key advanced applications in Telecom and Space fields.

II. Device Configuration

The proposed optical notch filter consists in a silicon-based microring resonator coupled to a single waveguide, integrated with a one-dimensional photonic crystal section, to form a PhCRR with radius R, as shown in Fig. 1(a). The portion of the ring resonator without the PhC has a length L_1. The waveguide has a rib structure with a width w_{wg} = 500 nm and a thickness $t_{wg,}$ = 200 nm, on a 50 nm thick slab layer The rib waveguide has been assumed fully embedded in silicon dioxide with a 1 μm thick overlayer and a substrate 3 μm thick (Fig. 1(b)). This waveguide configuration has been chosen because of its suitability for the selected tuning mechanism [23], enabling low loss values for the tuning [24]. The PhC section is made by a sidewall grating (Fig. 1(c)), formed by a width modulation of the waveguide, having a maximum w_{max} and minimum w_{min} width, with a duty-cycle DC. The values of the grating period Λ, w_{max} and w_{min} are 304 nm, 500 nm and 400 nm, respectively, to achieve the operating wavelength around 1550 nm. We have considered the fundamental TE_0 mode (Fig. 1(d)), which shows less scattering than the TM_0 mode. The values of w_{max} and w_{min} have been designed to avoid the excitation of higher order modes that could affect the filter operation. As it will be described in the following section, the PhC section includes a number of defects with a width w_{def} equal to w_{max} and a length L'_{def} (see Fig.1(c)).

We have adopted the electro-optical tuning mechanism due to the typical fast reconfigurability. A p-i-n junction has been considered in the regions of defects, with n+ and p+ doped regions (inset of Fig. 1(a)). The distance w_{dis} larger than 1 μm between the doped regions and the rib allows to neglect the losses due to the ion implantation [25]. As it is well known, the introduction of a defect into the PhC generates a resonance into the photonic bandgap. The resonance tuning is realized by changing the effective index in the defect sections by varying the applied voltage at the p-i-n junctions. The propagation loss of the unperturbed waveguide at λ = 1550 nm for the TE_0 mode is assumed equal to α = 5.1 dB/cm [26]. Although in literature lower values of propagation loss have been reported for the same waveguide [27], the choice to assume a propagation loss value (5.1 dB/cm) that is one order of magnitude higher than the state-of-the-art is a conservative approach, aiming at taking into account possible additional losses due to the grating fabrication. The tuning loss has to be added to this value in correspondence of the defects.

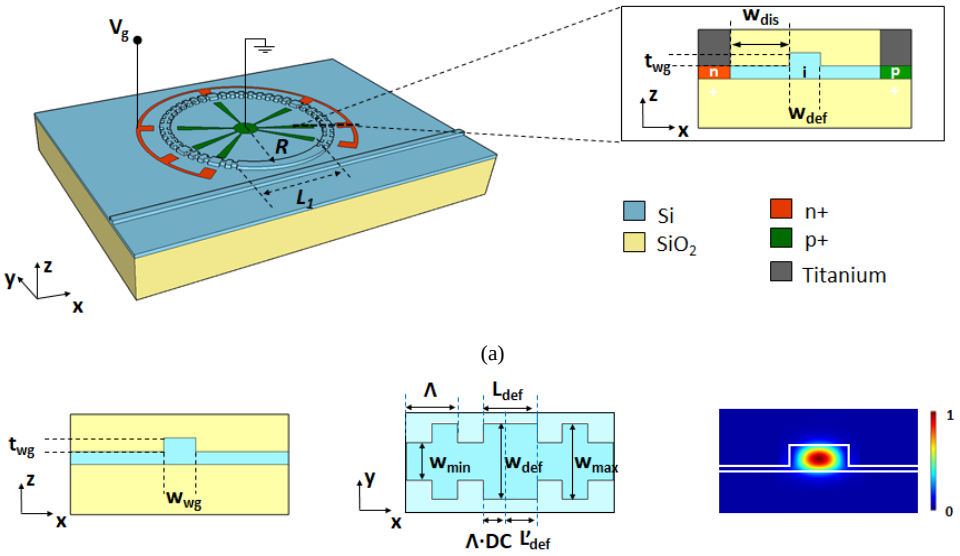

Fig. 1. (a) Schematic of the photonic crystal ring resonator with Newton distribution of the defects. Inset: Cross-section of the defect region into the PhC section. (b) Cross-section of the waveguide without PhC. (c) Top-view of the sidewall grating superimposed along a section of the ring resonator. (d) Normalized Poynting vector of TE_0 mode into the unperturbed waveguide cross-section.

III. Modelling and Design Technique of the PhCRR

The defects inside the PhC sections allow to achieve a flat bottom band of the notch filter response. In particular, a single defect inside a periodic structure determines a single resonance into the photonic bandgap (PBG). This defect gives rise to localized photonic states inside the PBG, as Fabry-Perot resonances, created by the lattice perturbation, and they can be used as functional elements for photonic devices. By including this structure inside a ring resonator and designing the resonator to match the resonance condition into the PBG, the transmission frequency response shows a pass-band behaviour, due to the presence of a Lorentzian-shaped peak inside the ring resonator spectrum [28]. The resonator reflectivity supports the use of this device as a notch optical filter with a Lorentzian response. In order to avoid the optical interference between the filtered and the unfiltered signal, this approach requires a circulator before the resonator [29], and this causes a large footprint and high chip complexity.

A Gaussian shape of the spectral response of the PhCRR with a flat bottom band could be achieved by engineering the position of the defects inside the PhC. In fact, by shaping the PhC spectrum, it is possible to tailor the PhCRR spectral response. According to [30], the insertion of multiple defects into the PhC causes the creation of coupled resonant cavities. Light can propagate in the PBG structure from one cavity to the next one, resulting in a transmission spectrum with a number of peaks in the resonance ripple equal to the number of the defects. This behaviour is due to the interactions between the evanescent cavity modes. To equalize the transmission spectrum of the PhCRR, assuming the position of the defects according to the Newton binomial series, a binomial distribution of resonances centered at the Bragg wavelength is expected to be generated, with a resulting flat band response. This approach derives from the well-known antenna theory. It has been demonstrated [31] that the ripple in radiation pattern can be limited or even suppressed choosing the feeding currents of a binomial antenna array, according to the Newton binomial series coefficients. The introduction of N_d defects inside the PhC with a total number of semi-periods N_t, entails the creation of $N_{sections}$ ($N_{sections} = N_d + 1$), with the length of each section defined by the Newton binomial rule. The length of the n^{th} grating section, where n is an integer number ($n \in [0{:}N_d]$), depends on the product of the coefficients B_n, corresponding to the coefficients of a generic binomial $(a+b)^{N_d}$), shown in the Pascal triangle (Table I), and on the ratio $N_t/\sum_{n=1}^{N_d} B_n$ [32]. In Fig. 2(a), we report, as an example, the sketch of a sidewall grating based on the silicon rib waveguide above described, with defects placed according to Table I, with $N_d = 6$ and $N_t = 128$.

TABLE I
Pascal Triangle of Binomial Coefficients B_N Related to the Number of Defects N_D inside the PhC.

N_d	B_n													
0							1							
1						1		1						
2					1		2		1					
3				1		3		3		1				
4			1		4		6		4		1			
5		1		5		10		10		5		1		
6	1		6		15		20		15		6		1	
7	1	7		21		35		35		21		7		1

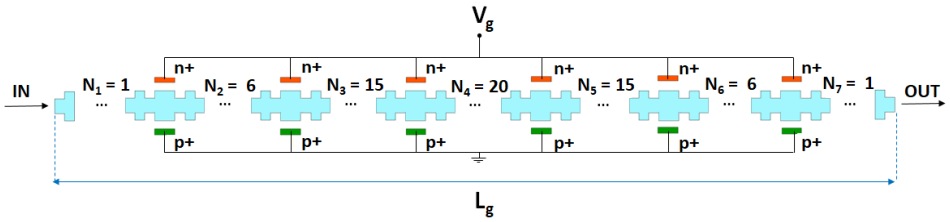

(a)

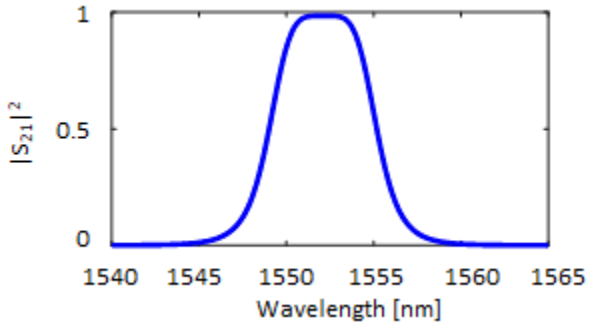

(b)

Fig. 2. (a) Silicon-based sidewall grating with defects placed according to the Newton rule; (b) Transmission spectrum of the PhC section with L_{def} = 3.11 µm, N_d = 6 and N_t = 128.

The defect region with a total length L'_{def} consists of a grating semi-period, with a width w_{max} and a length $\Lambda \cdot DC$, and a waveguide portion, with a width w_{max} and a length L_{def} used as discontinuity of the grating periodicity (Eq.1). $L'_{def,}$ is the same for all defects and L_{def} has been designed in order to achieve a target operating wavelength at 1550 nm, under Bragg conditions:

$$L'_{def} = DC \cdot \Lambda + L_{def} \quad (1)$$

$$L_{def} = \frac{4m+1}{4} \frac{\lambda_B}{n_{eff\text{-}def}} \quad m = 1, 2, \ldots \quad (2)$$

where λ_B is the Bragg wavelength and $n_{eff-def}$ is the effective refractive index of the defect region. With m = 5 and DC = 50%, we have obtained L_{def} = 3.11 µm, which corresponds to a total grating length $L_g \approx$ 38.27 µm, for N_d = 6 and N_t = 128. A single resonance inside the PBG can be observed for $5 < m < 50$. By increasing the m value ($m > 50$), multiple resonances appear into the PBG. The device electromagnetic behaviour has been investigated by using the effective index method [33]. The Transfer Matrix Method (TMM) [34] has been used to estimate the reflection and transmission of the grating through the *S*-parameters. Each defect and semi-period of the grating have been modelled as a 4x4 transmission matrix, as described in [35]. Assuming the defects distribution in the grating as reported in Table I, the final expression of the transmission matrix related to the whole structure is obtained by multiplying the transmission matrix of each single element (semi-periods and defects). Moreover, the transmission matrix has been replaced by a scattering matrix, according to [34], in order to evaluate both the transmission (S_{21}) and the reflection (S_{11}) of the PhC session. To simplify the analytical approach, the grating has been assumed symmetric, which corresponds to the condition $S_{21} = S_{12.}$

The grating transmission spectrum ($|S_{21}|^2$) is reported in Fig. 2(b), where a Gaussian flat top behaviour is clearly shown, given by the overlap between the Lorentzian-like resonances caused by each defect.

The tuning of the PhC response (Fig. 2(a)) can be obtained by injecting carriers using a p-i-n structure embedded into the defects. The spectral response is affected by the effective index change of the defects section, where a voltage V_g is applied to the junction. By using the drift diffusion equations [36], we have calculated the carrier density into the cross-section of the p-i-n junction (inset in Fig. 1(a)), when the applied voltage changes. The index change has been simulated as in [37] and the effective index (blue curve in Fig. 3) and the related losses (red curve in Fig. 3) have been calculated by using the Finite Element Method (FEM). The effective index change Δn_{eff}, increases as V_g increases, but at the expenses of higher value of losses. The device spectra of the PhC section have been calculated adding the tuning loss α_{tuning} to the waveguide losses, reported in Paragraph II, in correspondence to the defects.

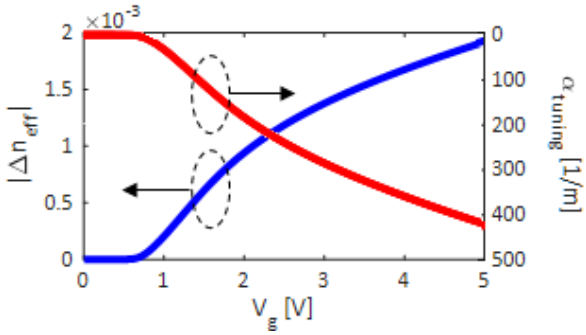

Fig. 3. Silicon-based rib waveguide: (Blue curve) trends of effective index change Δn_{eff}, and (Red curve) tuning loss α_{tuning} [1/m], as function of the applied voltage V_g.

The effect of the electro-optical tuning on the spectrum of the PhC under study is reported in Fig. 4(a)-(b). By increasing the applied voltage, a blue-shift of the central frequency f_c, with respect to its value at V_g = 0 V, $f_0 \approx$ 193.223 THz, has been obtained, as shown in Fig. 4(c), with a frequency detuning $\delta f_c = f_c - f_0$ as a funcion of V_g, with trend similar to Δn_{eff}, already shown in Fig. 3.

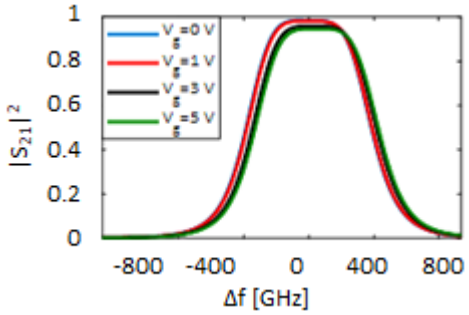

(a)

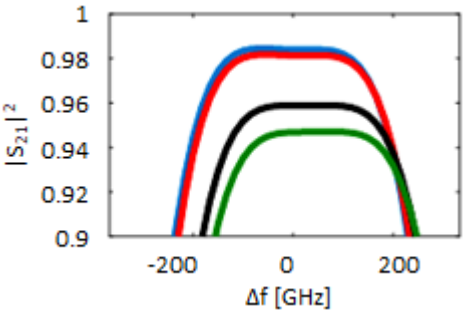

(b)

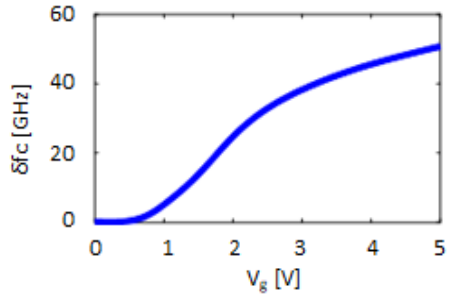

(c)

Fig. 4. Silicon-based sidewall grating with defects placed according to the Newton rule: (a) transmission spectra vs Δf, which is the frequency shift from the operating frequency ($f_0 \approx$ 193 THz); (b) inset of transmissions spectra vs Δf, (c) central frequency detuning, δf_c, as a function of V_g.

By including the above described PhC section into a microring resonator, a Gaussian-shape notch response can be achieved. We have modelled and calculated the transfer function T of the PhCRR by imposing the continuity conditions of the fields at the interfaces between the coupling region and the PhC section:

$$T = \frac{S_{21}k^2 e^{\varphi} e^{i\theta} + \tau \cdot (k^2 det\boldsymbol{S_{PhC}} e^{2i\theta} + 1)}{\tau(S_{12}+S_{21}) e^{\varphi} e^{i\theta} + \tau^2 e^{2i\theta} det\boldsymbol{S_{PhC}} - e^{2\varphi}} \qquad (3)$$

where k is the coupling coefficient (no loss into the coupling region has been assumed), $\tau = \sqrt{1-k^2}$, $\theta = \beta_{portion} \cdot L_1$, $\varphi = \alpha \cdot L_1$; $\beta_{portion}$ is the real part of the propagation constant related to L_1, α is the waveguide propagation loss [dB/cm].

The PhC section with length L_g, is described by a scattering matrix, S_{PhC}, whose parameters S_{ij} (i,j = 1,2) have been numerically calculated using the aforementioned approach.
To obtain the constructive wave interference between the PhC section and the unperturbed ring resonator section, the following equation must be satisfied at the operating wavelength:

$$\angle S_{21} + \theta = 2m\pi \qquad m = 1, 2, \ldots \qquad (4)$$

Furthermore, in order to increase the coupling efficiency, L_1 is assumed longer than the coupling length (i.e. more than 20% of the PhCRR length), according to a conservative approach:

$$L_1 \geq 0.2 \cdot (L_1 + L_g) \qquad (5)$$

The length L_1 can be derived by Eqs. 4-5 and it also depends on the ring radius. A minimum PhCRR radius R = 5 µm has been assumed, because for $R \geq$ 5 µm the bending losses can be neglected [38]. For example, by integrating the PhC section into the ring resonator, as shown in Fig. 2(a), we have obtained L_1 = 10.066 µm and a ring radius R = 7.7 µm.

In order to achieve a proper operation of the notch filter, the value of k results a crucial parameter. In particular, k^2 represents the power coupling efficiency inside the coupling region. According to [39], we have calculated the critical value of the coupling coefficient $K_{critical}$ = 15.3 %, corresponding to the transmission power equal to zero for the configuration under investigation. Figure 5 shows the magnification on the bottom band of the notch response for several k^2 values. For values around $K_{critical}$ (k^2 = 15 % - 16 %), the notch behaviour shows a Gaussian profile, with a very small ripple values for k^2 = 15 % (as shown in the inset of Fig. 5) and null ripple for k^2 = 16 %. For $k^2 << K_{critical}$ (k^2 = 10 %), high ripple values are observed into the band, while for $k^2 >> K_{critical}$ (k^2 = 20 %) the notch response has a Lorentzian-like shape with no-flat bottom band.

As for the phase of the transmission response, for $k^2 \approx K_{critical}$, the phase shows a linear trend at the operating frequency. The linearizing effect of the phase response is shown at $\angle T = 0$ for $k^2 \leq K_{critical}$ (Fig. 6(a)) and at $\angle T = \pi$ for $k^2 \geq K_{critical}$ (Fig. 6(c)), as highlighted into the insets referred to the red dotted boxes. To exploit this effect, a proper design of the photonic crystal region is required. By imposing $\angle S_{12} \equiv \angle S_{21} = 0$, we have estimated the contour plots of the PhCRR transmission phase, depending on the phase of S_{11} and S_{22}.

The PhC design conditions have been derived by the contour plots, in order to obtain both a linear phase response at $\angle T = 0$ for $k^2 \leq K_{critical}$ (Fig. 6(b)) and $\angle T = \pi$ for $k^2 \geq K_{critical}$ (Fig. 6(d)), and then, a flat bottom transmission spectrum.

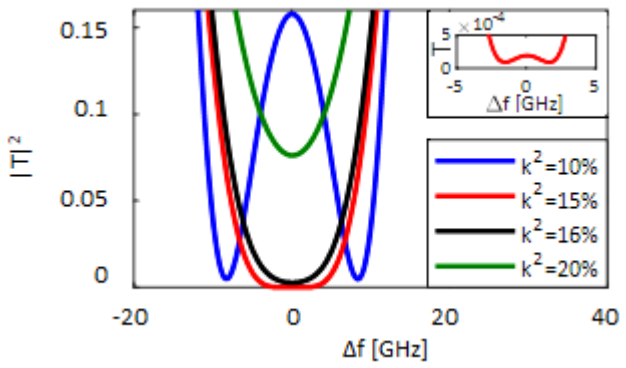

Fig. 5. Bottom band of the PhCRR transmission response, for several values of coupling efficiency k^2.

In particular, the condition $\angle S_{11} = \angle S_{22}$ (described by the central diagonal white line in Fig. 6(b)-(d)) ensures to satisfy the requirement $\angle T = \pi$ for $k^2 \geq K_{critical}$, even if it leads $\angle T = \pi$ also for $k^2 \leq K_{critical,,}$ that is not compliant with the design requirement ($\angle T = 0$). Then, the PhC section must satisfy both the following conditions:

$$\angle S_{12} = \angle S_{21} = 0 \quad (6)$$

$$|\angle S_{11} - \angle S_{22}| = \pi \quad (7)$$

with Eq. 7 corresponding to the blue lines in Fig. 6(b) for $k^2 \leq K_{critical}$ and to the symmetrical white lines with respect to the diagonal in Fig. 6(d) for $k^2 \geq K_{critical}$. If the number of defects is odd, the PhC must be ended with a semiperiod, while if the number of defects is even, some grating periods must be added to keep the phase symmetry. Furthermore, if some manufacturing issues affects L_1 and then if the condition in Eq. 4 is not satisfied anymore, a shift of the filter central frequency occurs, resulting in a Lorentzian-shape with a high ripple into the stopband, as shown in Fig. 7.

The conditions defined by Eqs. 6,7 have been assumed for the design of the PhCRR and the corresponding transmission spectrum is reported in Fig. 8(a). The resonance at the operating frequency (f_0 = 193.223 THz) shows a bandwidth B = 32.82 GHz and a Gaussian profile. The other resonances have a Lorentzian profile with Fano behaviour. Gaussian resonance has an extinction ratio (ER) > 40 dB and a filter slope of about 2.62 dB/GHz, measured between 90% and 10% of the transmission spectrum. A largely flat stopband has been obtained with k^2 = 16 % (see Fig. 8(d)), while a ripple equal to 0.33 dB can be observed for k^2 = 15 % (see Fig. 8(c)). The matching of the transmission spectrum of the optical filter with a Gaussian fitting has been confirmed by a root-mean-square error for the Gaussian fitting ($RMSE_{gauss}$) that is one order of magnitude lower than the error ($RMSE_{Lorentz}$) obtained by fitting with a Lorentzian profile.

Nowadays, a mature manufacturing technique is available to realize the proposed PhCRR. The device, based on silicon technology platform, can be manufactured by using electron-beam lithography followed by reactive ion plasma etching. The doped region n+ and p+ can be defined with lithography and phosphorous and boron implantation, respectively. The cover layer in silicon dioxide can be deposited by plasma-enhanced chemical vapour deposition followed by an annealing process for the dopants activation.

Furthermore, for the detection of the PhCRRs' phase and intensity spectra, the optical single sideband modulation vector analysis ensures an accurate measurement of the filter responses, with resolution less than 0.1 MHz [40].

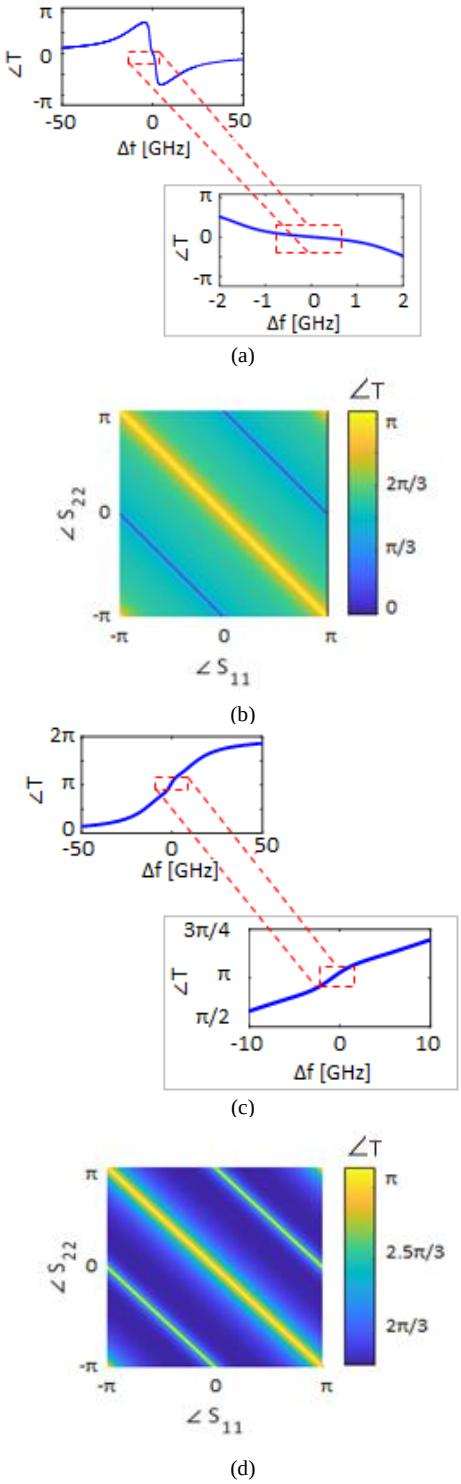

Fig. 6. Phase response of PhCRR for (a) $k^2 \leq K_{critical}$ and (c) $k^2 \geq K_{critical}$, and phase transmission $\angle T$ contour map depending on S_{11} and S_{22} to achieve a phase linear response null at 0 (b) or π (d).

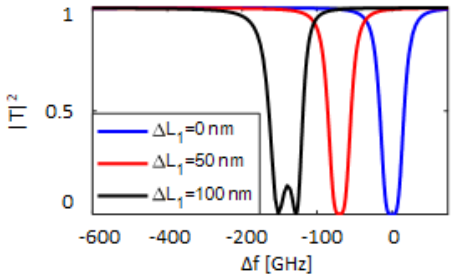

Fig. 7. PhCRR transmission as function of Δf at three different values of ΔL_1.

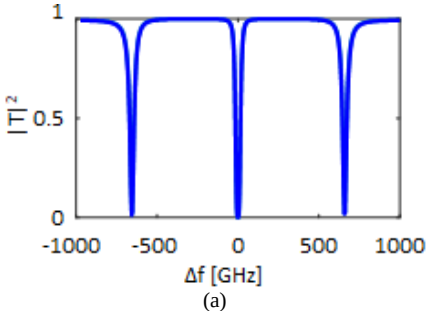

(a)

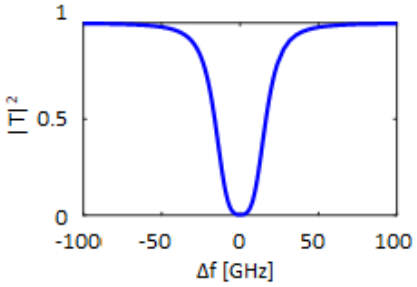

(b)

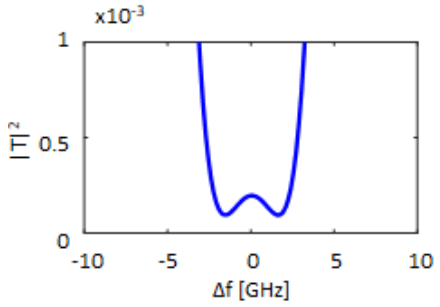

(c)

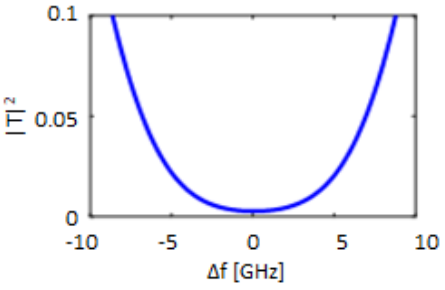

(d)

Fig. 8. Wide transmission spectrum of PhCRR under investigation (a), with a zoom on the Gaussian-like resonance (b). Magnification on the bottom band for k^2 = 15% (c) and k^2 = 16% (d).

IV. Design Results

The PhC section has been designed to obtain the best compromise in terms of *B*, *ER*, tuning range and band flatness to optimize the performance of the proposed notch filter based on a PhCRR,as explained in Section III.

Several simulations have been carried out on the semi-periods number N_t, defects number N_d and defects lengths L_{def} of the Newton-based sidewall gratings. According to the PhC design procedure as in Section 3, we report the transmission spectra of the gratings with N_t = 128 and N_t = 256, for different values of N_d (L_{def} = 3.11 µm), in Fig. 9(a) and Fig. 9(b), respectively. The maximum number of defects in the grating strictly depends on the fulfilment of the Newton rule (Table I). The number of binomially distributed defects N_d is a fundamental parameter to increase the pass-band equalization and the *ER*, without reducing significantly the bandwidth. Furthermore, by comparing the spectra with the same N_d, the configuration with N_t = 256 provides an enhancement of the bandwidth compared to the configuration with N_t = 128. According to the condition of N_t equal to a power of 2, a minimum value of N_t = 128 has been taken into account in order to avoid PhCRR configurations with R < 5 µm, so preventing the increase of the optical losses [38]. Moreover, a number of semiperiods N_t > 256 (i.e. N_t = 512 - 1024) provides a maximum transmission of about 0.1, which makes difficult to estimate the Gaussian trend.

The performance of the most promising PhC, and PhCRR configurations have been summarized in Table II, highlighting the influence of the PhC section on the PhCRR performance. The PhCRR configurations have been designed following the criteria defined by the Eqs. 4-7, with a Newtonian distribution of the PhC defects and L_{def} = 3.11 µm, according to Table I.

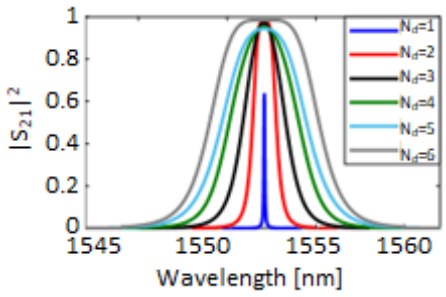

(a)

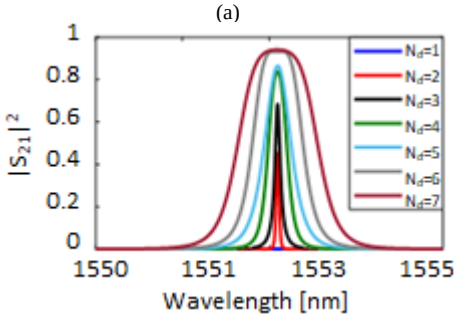

(b)

Fig. 9. Transmission spectra of silicon-based sidewall gratings with N_t = 128 (a) and N_t = 256 (b) and for several values of N_d (L_{def} = 3.11 µm), designed according to Table I.

TABLE II
DESIGN PARAMETERS OF SEVERAL PHC CONFIGURATIONS AND RELATED PHCRRS (L_{DEF} = 3.11 µM).

N_t	N_d	PhC			PhCRR				
		B [GHz]	$\|S_{12}\|^2$ (@ f_0)	$R_{lorentz/gauss}$	$K_{critical}$ [%]	R [µm]	B [GHz]	ER [dB]	$R_{lorentz/gauss}$
128	2	171.20	0.970	2.46 x 10^2	~16	5.18	14.48	28.36	2.55 x 10^1
128	3	311.45	0.973	9.43 x 10^1	~20	5.84	35.21	38.82	2.16 x 10^1
128	4	507.62	0.953	5.24 x 10^1	~32	6.50	69.08	57.13	2.25 x 10^1
128	5	621.92	0.943	2.60 x 10^1	~36	7.06	82.57	37.56	2.95 x 10^1
128	6	774.64	0.984	2.50 x 10^2	~16	7.70	32.94	25.68	2.23 x 10^1
256	4	30.45	0.837	1.32 x 10^2	~31	10.35	8.29	23.41	1.22 x 10^1
256	5	43.92	0.864	1.19 x 10^2	~36	11.01	15.04	49.33	3.59 x 10^1
256	6	75.87	0.932	2.22 x 10^2	~14	11.57	6.40	18.48	1.15 x 10^1
256	7	117.79	0.940	2.92 x 10^2	~20	12.14	10.43	41.25	1.41 x 10^1

As shown in Table II, $K_{critical}$ strongly depends on the value of the transmission of the PhC at the operating frequency and on the PhCRR radius R. The performance of the PhC and PhCRR strictly depends on the critical value $K_{critical}$, which is mostly affected by the geometrical parameters, such as N_t and N_d.

According to [41], low values of $K_{critical}$ are necessary to obtain a narrow bandwidth, at the expense of the ER. Using a Lorentzian and Gaussian fitting, the ratio $R_{lorentz/gauss}$ between $RMSE_{lorentz}$ and $RMSE_{gauss}$ has been used to estimate how much the transmission profile approaches a perfect Gaussian one. In particular, for $R_{lorentz/gauss}$ > 10, the resonance fits perfectly with a Gaussian shape. Furthermore, the enhancement of the bandwidth of about one order of magnitude is obtained when the PhC and PhCRR results are compared, at the expense of a decrease of $R_{lorentz/gauss}$. As expected, the most promising results on the PhCRR performance, in terms of bandwidth B and ER, i.e. B = 6.4 GHz and ER = 18.48 dB, have been achieved using the PhC configuration with N_t = 256, and N_d = 6 (see Table II).

The configurations with N_t = 256 and N_d = 4 or N_d = 6, are very sensitive to manufacturing errors: a deviation ΔL_1 = 10 nm causes significant ripple into the bottom band (for the configuration with N_t = 256 and N_d = 4) or an asymmetric-Lorentzian shape of the resonance (for the configuration with N_t = 256 and N_d = 6). Therefore, a notch filter very insensitive to possible technological issues cannot be manufactured in one of those configurations.

Aiming at obtaining a narrow bandwidth, we consider that the increase of the defects lengths L_{def}, according to Eq. 2, provides a bandwidth improvement. For instance, in Fig. 10 the transmission response for the Newton-based sidewall grating as function of L_{def}, with N_t = 128 and N_d = 6 is shown. The values of L_{def} equal to 3.11 µm, 6.07 µm and 11.99 µm, (corresponding to m = 5, m = 10 and m = 20, respectively, in Eq. 2), have been considered to achieve the device operation close to 1550 nm. By increasing the m value of a factor 2, a B enhancement by a factor 1.5 is achieved, without affecting the Gaussian profile of the resonance.

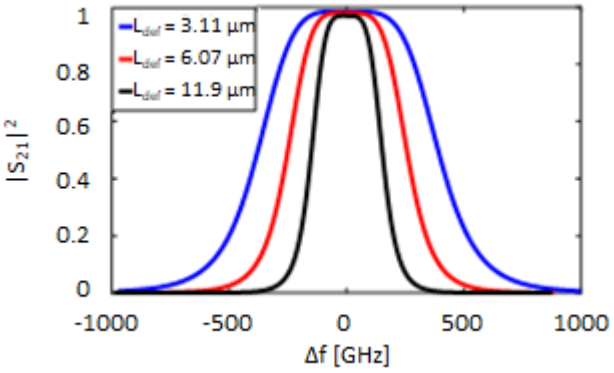

Fig. 10. Transmission spectra S_{21} of sidewall grating with N_t = 128 and N_d = 6 for several values of the L_{def}, compliant to Eq.2.

To investigate the impact of L_{def} on the PhCRR performance, a parametric analysis has been carried out to satisfy the requirements of narrow bandwidth and high extinction ratio, in order to maximize the figure of merit (*FOM*), defined as *FOM* = *ER*/*B* (expressed in dB/GHz). The configurations assumed are with N_t = 256 and with N_d = 5 and N_d = 7. The behaviour of the *FOM* and R as a function of L_{def} has been reported in Fig. 11, where the dotted points are referred to the L_{def} values compliant to Eq. 2.

A maximum value of *FOM* has been obtained with L_{def} = 3.11 µm for both configurations. Although an enhancement of the bandwidth has been obtained for larger L_{def} values, a *FOM* decrease has been observed, caused by a worsening of *ER*. Therefore, the condition L_{def} = 3.11 µm represents the best solutions to achieve a narrow bandwidth with high *ER*, maximizing the *FOM* value with higher footprint. In particular, the PhCRR with N_t = 256, N_d = 5 and L_{def} = 3.11 µm provides B = 15.04 GHz, *ER* = 49.33 dB with R = 11.01 µm, while PhCRR with N_t = 256, N_d = 7 and L_{def} = 3.11 µm leads to B = 10.43 GHz, *ER* = 41.25 dB with R = 12.14 µm.

TABLE III
TUNING PERFORMANCE COMPARISON (ER_{MAX} = ER @ V_G = 0 V, ER_{MIN} = ER @ $V_G = V_{MAX}$).

N_t	N_d	L_{def} [µm]	$K_{critical}$ [%]	B [GHz]	V_{max} [V]	δf_c [GHz]	ER_{max} [dB]	ER_{min} [dB]
256	5	3.11	36	15.04	1.69	18.65	49.98	26.72
256	7	3.11	20	10.43	1.50	15.18	41.25	25.46

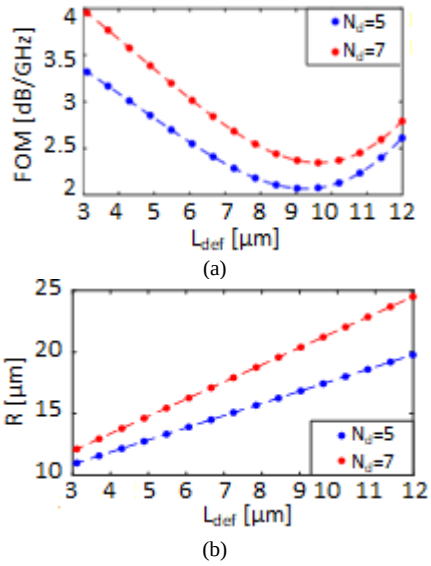

Fig. 11. (a) Figure-of-merit *FOM* (*ER*/*B*); (b) PhCRR radius R as a function of L_{def}, for PhCRRs with N_t = 256 and N_d = 5 (blue curve), and N_d = 7 (red curve). The dotted points refer to defects lengths L_{def} that are compliant to Eq. 2.

Applying a voltage V_g to the p-i-n junctions, a resonance blue-shift can be observed. Table III shows a summary of the tunable PhCRRs performance. The maximum applied voltage V_{max} is estimated in order to keep a Gaussian-like response with a maximum worsening of the bandwidth equal to 10 %, with respect to the value at V_g = 0 V. As the applied voltage increases, a blue frequency shift (δf_c) of the resonance has been detected with the *ER* decrease, assuming the PhC section compliant with Eq. 4 at V_g = 0 V. A large δf_c value has been achieved of about18 GHz with a minimum ER value ER_{min} > 26 dB, and 15 GHz with ER_{min} > 25 dB, for N_d = 5 and N_d = 7, respectively, satisfying the requirements of the notch filter applications. Furthermore, assuming an initial condition V_g = 0.6 V, a fine tuning of the central frequency is achieved, as shown in Fig. 12, with the same behaviour of Fig. 3(b). A higher curve slope, and then a higher tuning efficiency, has been observed for N_d = 7 with respect to N_d = 5. Taking into account the bandwidth and the tuning range, the PhCRR with N_t = 256, N_d = 7 and L_{def} = 3.11 µm represents the best compromise to achieve a performing Gaussian notch filter with flat band.

We have calculated that the coupling efficiency between the bus waveguide and the ring portion without grating with length L_1 has to be 20% for the selected configuration. This value ensures a Gaussian filtering shape, avoiding ripple into the pass-band.

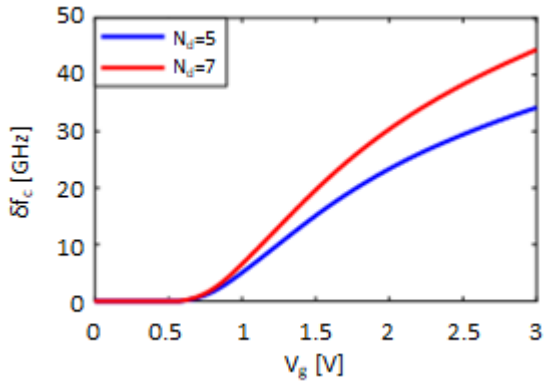

Fig. 12. Detuning, δf_c, of the central frequency of the notch filter vs applied voltage V_g.

With R = 12.14 µm, and L_1 = 15.392 µm, that is about 20% of the PhCRR perimeter, by using a 2D Finite Difference Time Domain (FDTD) approach, we have estimated the coupling efficiency as a function of the gap g between the bus and the ring (Fig. 13). In particular, the coupling efficiency is equal to 20% for g = 116 nm. If the value of the coupling efficiency slightly moves from the nominal value (k^2 = 19 %), a maximum ripple of about 0.2 dB is observed.

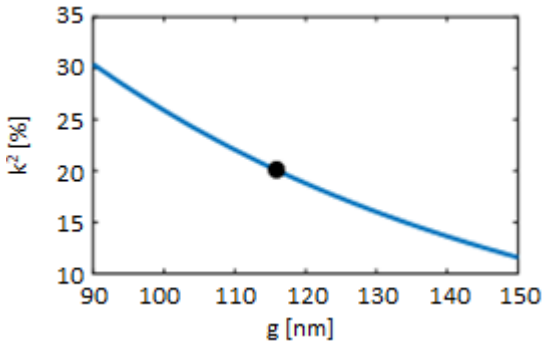

Fig. 13. Coupling efficiency k^2 [%] vs gap bus-ring g [nm].

The transmission spectrum of the tuneable Newton-based PhCRR with N_t = 256, N_d = 7 and L_{def} = 3.11 µm is reported in Fig. 14. In Fig. 14(a) it is shown a calculated Gaussian profile with a flat bandwidth (B = 10.43 GHz), high *ER* (41 dB) and high slope of the sidewalls of the spectrum (2.62 dB/GHz). In particular, the behaviour of 1st order Butterworth notch filter has been obtained, with a slope of 20 dB per decade and maximally flat stopband, as shown in Fig. 14(b). Furthermore, a fine, continuous and quasi-linear tuning of the central frequency has been obtained by applying a voltage on the p-i-n junction at the defects from 0.6 V to 1.5 V, with a slope of 20.17 GHz/V (Fig. 14(c)-(d)), and a minimum *ER* = 25 dB. A maximum detuning of the central frequency of about 15 GHz has been achieved, without affecting the Gaussian shape of the resonance, with a power consumption of 47mW and reconfigurability time of about 1 ns. Such performance confirms the advantage of the carrier-injection tuning technique in terms of broad tunable-frequency range and fast reconfigurability.

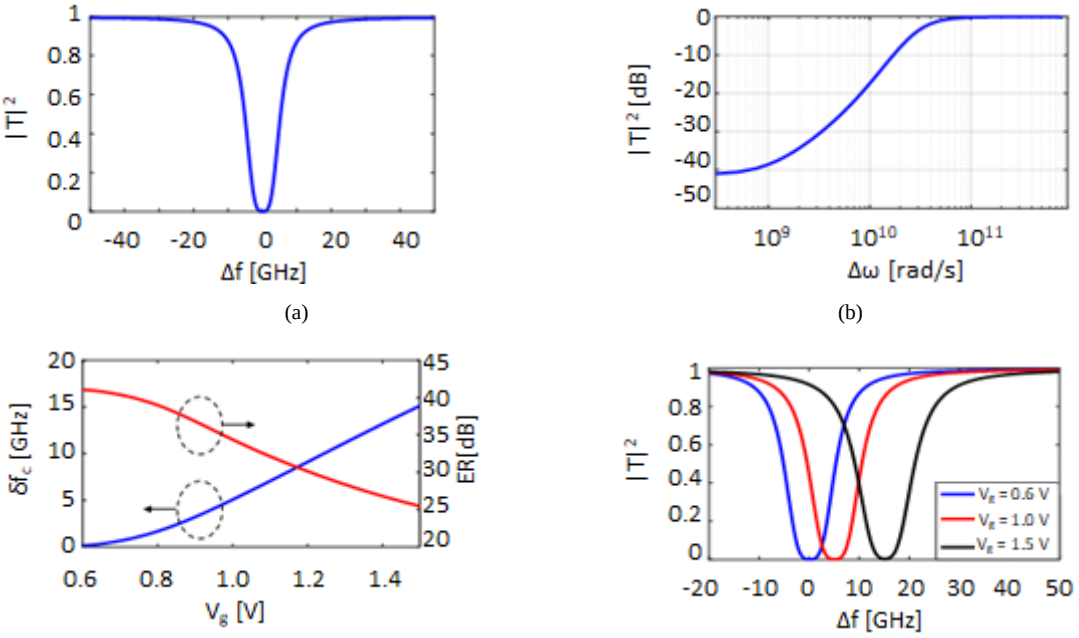

Fig. 14: (a) Transmission spectrum of the PhCRR with N_t = 256, N_d = 7, L_{def} = 3.11 µm (k^2 = 20%) and Bode plot (b) of the 1st order Butteworth low pass filter (ω is the angular frequency [rad/s] and $\Delta\omega$ is the angular frequency shift from the operating angular frequency). (c) Shifting of the central frequency and ER trends as a function of the applied voltage V_g, with some examples of the transmission spectra after voltage tuning (d) ($f_0 \approx$ 193.2877 THz).

V. Conclusion

A novel ultra-compact photonic-crystal ring resonator with a bandwidth B = 10.43 GHz and ER > 40 dB has been designed to be used as notch filter. The Newton distribution of the defects inside the photonic crystal section provides a Gaussian-shaped frequency response, with very steep sidewalls (2.62 dB/GHz). The integration of a p-i-n junction, in correspondence to the PhC defects, enables a continuous tuning of the central frequency (15 GHz), fast switching time (≈ 1 ns) with a power consumption equal to about 47 mW. Our device is a clear improvement of the state-of-the-art, in terms of stopband equalization, monolithic integration capability, wide band tunability, low power consumption, very short switching time, and ultra- small footprint. The applications of the proposed notch filter are in the field of telecom and microwave photonics, for next-generation wireless networks and telecom payloads in space applications, since it meets advanced requirements, such as compactness, wide range tunability, fast reconfigurability, relatively low power consuming and multi-users management.

References

[1] C. K. Madsen and J. H. Zhao, *Optical filter design and analysis*, New York: Wiley, 1999.

[2] J. Capmany and D. Novak, "Microwave photonics combines two worlds," *Nat. Phot.*, vol. 1, no. 6, pp. 319, 2007.

[3] J. Yao, "Photonics to the rescue: A fresh look at microwave photonic filters," *IEEE Micro. Mag*., vol. 16, pp. 46–60, 2015.

[4] J. Capmany, B. Ortega and D. Pastor, "A tutorial on microwave photonic filters," *J. Lightwave Tech*., vol. 24, no. 1, pp. 201–229, 2006.

[5] D. Novak, R. B. Waterhouse, A. Nirmalathas, C. Lim, P. A. Gamage, T. R. Clark, M. L. Dennis and J. A. Nanzer, "Radio-over-fiber technologies for emerging wireless systems," *IEEE J. Quantum El*., vol. 52, no. 1, pp. 1-11, 2016.

[6] C. Ciminelli, F. Dell'Olio and M. N. Armenise, *Photonics in Space: Advanced Photonic Devices and Systems*, Singapore: World Scientific, 2016.

[7] F. Dell'Olio, G. Brunetti, D. Conteduca, N. Giovinazzi, N. Sasanelli, C. Ciminelli and M. N. Armenise, "Integrated Microwave Photonics: Overview and Promising Space Applications,", in *International Conference on Applications in Electronics Pervading Industry, Environment and Society*, ed. Springer, Cham, 2017.

[8] L. Gao, X. Chen and J. Yao, "Tunable microwave photonic filter with a narrow and flat-top passband," *IEEE Micro. Wir. Comp. Lett.*, vol. 23, no. 7, pp. 362-364, 2013.

[9] D. Marpaung, B. Morrison, M. Pagani, R. Pant, D.-Y. Choi, B. Luther-Davies, S. J. Madden and B. J. Eggleton, "Low-power, chip-based stimulated Brillouin scattering microwave photonic filter with ultrahigh selectivity," *Optica*, vol. 2, no. 2, pp. 76-83, 2015.

[10] J. S. Fandiño, P. Muñoz, D. Doménech and J. Capmany, "A monolithic integrated photonic microwave filter," *Nat. Phot*., vol. 11, no. 2, pp. 124-129, 2017.

[11] W. Zhang and J. Yao, "A silicon photonic integrated frequency-tunable microwave photonic bandpass filter," in *Proc. 2017 International Topical Meeting on Microwave Photonics (MWP)*, Beijing, China, 2017, pp. 1-4.

[12] P. Dong, W. Qian, H. Liang, R. Shafiiha, D. Feng, G. Li, J. E. Cunningham, A. V. Krishnamoorthy and M. Asghari, "Thermally tunable silicon racetrack resonators with ultralow tuning power," *Opt. Express*, vol. 18, no. 19, pp. 20298-20304, 2010.

[13] P. Dong, N. N. Feng, D. Feng, W. Qian, H. Liang, D. C. Lee, B. J. Luff, T. Banwell, A. Agarwal, P. Toliver, R. Menendez, T. K. Woodward and M. Asghari, "GHz-bandwidth optical filters based on high-order silicon ring resonators," *Opt. Express*, vol. 18, no. 23, pp. 23784-23789, 2010.

[14] F. Xia, M. Rooks, L. Sekaric and Y. Vlasov, "Ultra-compact high order ring resonator filters using submicron silicon photonic wires for on-chip optical interconnects," *Opt. Express*, vol. 15, no. 19, pp. 11934-11941, 2007.

[15] P. A. Morton, J. B. Khurgin, Z. Mizrahi and S. J. Morton, "Commercially packaged optical true-time-delay devices with record delays of wide bandwidth signals," in *Proc. 2014 Conference on Lasers and Electro-Optics (CLEO)*, San Jose, CA, USA, 2014, pp. 1-2.

[16] M. Huang, S. Li, M. Xue, L. Zhao and S. Pan, "Flat-top optical resonance in a single-ring resonator based on manipulation of fast-and slow-light effects," *Opt. Express*, vol. 26, no. 18, pp. 23215-23220, 2018.

[17] C. Errando-Herranz, F. Niklaus, G. Stemme and K. B. Gylfason, "Low-power microelectromechanically tunable silicon photonic ring resonator add-drop filter," *Opt. Lett*., vol. 40, no. 15, pp. 3556-3559 (2015).
[18] I. Giuntoni, A. Gajda, M. Krause, R. Steingrüber, J. Bruns and K. Petermann, "Tunable Bragg reflectors on silicon-on-insulator rib waveguides", *Opt. Express*, vol. 17, no. 21, pp. 18518-18524, 2009.
[19] K. Chen, F. Duan and Y. Yu, "High-performance thermo-optic tunable grating filters based on laterally supported suspended silicon ridge waveguide," *Opt. Express*, vol. 26, no. 15, pp. 19479-19488, 2018.
[20] A. D. Simard and S. LaRochelle, "Complex apodized Bragg grating filters without circulators in silicon-on-insulator," *Opt. Express*, vol. 23, no. 13, pp. 16662-16675, 2015.
[21] J. Jiang, H. Qiu, G. Wang, Y. Li, T. Dai, X. Wang, H. Yu, J. Yang and X. Jiang, "Broadband tunable filter based on the loop of multimode Bragg grating," *Opt. Express*, vol. 26, no. 1, pp. 559-566, 2018.
[22] M. G. Saber, Y. Wang, E. El-Fiky, D. Patel, K. A. Shahriar, M. S. Alam, M. Jacques, Z. Xing, L. Xu, N. Abadia and D. V. Plant, "Transversely coupled Fabry–Perot resonators with Bragg grating reflectors," *Opt. Lett*., vol. 43, no. 1, pp. 13-16, 2018.
[23] Q. Xu, B. Schmidt, S. Pradhan and M. Lipson, "Micrometre-scale silicon electro-optic modulator," *Nature*, vol. 435, pp. 325-327, 2005.
[24] G. T. Reed, G. Z. Mashanovich, F. Y. Gardes, M. Nedeljkovic, Y. Hu, D. J. Thomson, L. Ke, P. Wilson, S.-W- Chen and S. S. Hsu, "Recent breakthroughs in carrier depletion based silicon optical modulators," *Nanophot*., vol. 3, no. 4-5, pp. 229-245, 2014.
[25] C. A. Barrios, V. R. Almeida, R. Panepucci and M. Lipson, "Electrooptic modulation of silicon-on-insulator submicrometer-size waveguide devices," J. *Lightwave Tech*., vol. 21, no. 10, pp. 2332-2339, 2003.
[26] Q. Xu and M. Lipson, "Carrier-induced optical bistability in silicon ring resonators," *Opt. Lett*., vol. 31, no. 3, pp. 341-343, 2006.
[27] S. K. Selvaraja, P. De Heyn, G. Winroth, P. Ong, G. Lepage, C. Cailler, A. Rigny, K. K. Bourdelle, W. Bogaerts, D. Van Thourhout, J. Van Campenhout and P. Absil, "Highly uniform and low-loss passive silicon photonics devices using a 300mm CMOS platform," in *Proc. Optical Fiber Communications Conference and Exhibition (OFC)*, San Diego, CA, USA, 2014.
[28] Y. M. Kang, A. Arbabi and L. L. Goddard, "Engineering the spectral reflectance of microring resonators with integrated reflective elements," *Opt. Express*, vol. 18, no. 16, pp. 16813-16825, 2010.
[29] C. Ciminelli, F. Dell'Olio, G. Brunetti, D. Conteduca and M. N. Armenise, "New microwave photonic filter based on a ring resonator including a photonic crystal structure," in *2017 Proc. 19th International Conference on Transparent Optical Networks (ICTON)*, Girona, Spain, 2017, pp. 1-4.
[30] A. Yariv, Y. Xu, R. K. Lee and A. Scherer, "Coupled-resonator optical waveguide: a proposal and analysis," *Opt. Lett.*, vol. 24, no. 11, pp. 711-713, 1999.
[31] S. Ramo and J. R. Whinnery, *Fields and waves in modern radio*, John Wiley & Sons, 1953.
[32] J. L. Coolidge, "The story of the binomial theorem," *The Am. Math. Mon*., vol. 56, no. 3, pp. 147-157, 1949.
[33] R. M. Knox and P. P. Toulios, "Integrated Circuits for the Millimeter Through Optical Frequency Range," *Proc. of MRI Symposium on Submillimeter Waves*, Polytechnic Press, 1970.
[34] M. Born and E. Wolf, *Principles of optics: electromagnetic theory of propagation, interference and diffraction of light*, Elsevier, 1980.
[35] G. Brunetti, D. Conteduca, F. Dell'Olio, C. Ciminelli and M. N. Armenise, "Design of an ultra-compact graphene-based integrated microphotonic tunable delay line," *Opt. Express*, vol. 26, no. 4, pp. 4593-4604, 2018.
[36] D. Vasileska, S. M. Goodnick and G. Klimeck, *Computational Electronics: semiclassical and quantum device modeling and simulation*, CRC press, 2016.
[37] R. Soref and B. Bennett, "Electrooptical effects in silicon," *IEEE J. Quantum Elec*., vol. 23, no. 1, pp. 123-129, 1987.
[38] Y. A. Vlasov and S. J. McNab, "Losses in single-mode silicon-on-insulator strip waveguides and bends," *Opt. Express*, vol. 12, no. 8, pp. 1622-1631, 2004.
[39] A. Yariv, "Critical coupling and its control in optical waveguide-ring resonator systems," *IEEE Phot. Tech. Lett*., vol. 14, no. 4, pp. 483-485, 2002.
[40] S. Pan and M. Xue, "Ultrahigh-Resolution Optical Vector Analysis Based on Optical Single-Sideband Modulation," *J. of Lightwave Technology*, vol. 35, no. 4, 2017.
[41] W. Bogaerts, P. De Heyn, T. Van Vaerenbergh, K. De Vos, S. Kumar Selvaraja, T. Claes, P. Dumon, P. Bienstman, D. Van Thourhout and R. Baets, "Silicon microring resonators," *Las. & Phot. Rev*., vol. 6, no. 1, pp. 47-73, 2012.